Chapter 3

Results

In this chapter we present the results of our investigations. This chapter consists of four sections. In the first section we present results for optimal control of time averaged quantities in simple quantum systems. The influence of relaxation on the shape of the optimal control field is investigated.

In the second section a ground state and excited states of strongly interacting few body quantum systems are calculated with a help of the QGA. As an example, we have investigated the formation and melting of a Wigner molecule in one and two dimensions.

In the third section we determine the optimal pulse shape in order to maximize the transfered charge through a double quantum dot. We investigate the influence of relaxation on the optimal control field and the role of interdot Coulomb repulsion.

In the fourth section we provide results of our simulations of the ultrafast cluster explosion of clusters under strong femtosecond laser fields. The correlation between charge state and kinetic energy of the ejected ion is investigated. We also study the influence of the cluster size on the mean and maximal kinetic energy of the ions after explosion.

3.1 Optimal control of a time averaged occupation of the excited level in a two-level system

In this section we study the influence of relaxation on the shape of the optimal field.

In the first subsection we perform numerical integration of the Euler-Lagrange equation (see Eq. [2.10]) for various parameters of relaxation. The influence of boundary conditions on the shape of the control field is also investigated.

In the second subsection we present numerical and analytical studies of the control problem using a simplified Lagrangian.

3.1.1 The influence of relaxation on the optimal control

In order to make a systematic study of the problem of control over a finite time interval that we have formulated in the Theory section [2.1], let us consider the optimal control of a two level system. We assume that initially the ground state of this system is occupied and the excited level is empty, i.e. $\rho_{11} = 1$ and $\rho_{22} = 0$. We are looking for the optimal shape of the field $V(t)$ that maximizes the mean occupation of the excited state ρ_{22} over time interval $t \in [0, T]$, or in other words, that maximizes $n_2 = \frac{1}{T} \int_0^T \rho_{22}(t) dt$. Therefore, we consider the objective functional density (see Eq. 2.4)

$$\mathcal{L}_{ob}(\rho(t)) = \rho_{22}(t)/T. \tag{3.1}$$

In the limit of a weak relaxation in the system, the expression for the occupation of the exited state ρ_{22} obtains a very simple form $\rho_{22} = \sin^2(\theta(t))$ within the Rotating Wave Approximation.

In this limit the corresponding Euler-Lagrange (EL) equation for the optimal pulse envelope $\theta(t)$ (see Eq. [2.10]) reads

$$-\lambda_1 \frac{d^4\theta}{dt^4} + \lambda \frac{d^2\theta}{dt^2} - \frac{\mu^2}{2T} \sin(2\theta) = 0. \tag{3.2}$$

Here, we use the boundary conditions $\theta(0) = \dot{\theta}(0) = \dot{\theta}(T) = 0$ and $\theta(T) = \pi/2$, that guarantees maximization of the population ρ_{22}. Eq. [3.2] is known as a limiting case of the dispersive sine-Gordon equation and it is exactly integrable [63]. In the presence of decoherence ($\gamma_1, \gamma_2 \neq 0$) we use the explicit formula for the $\rho_{22}(t)$ given by Eq. [2.16] and then solve the corresponding EL equation by standard numerical techniques, for example using the fourth order Runge-Kutta method [71].

We have calculated the optimal pulse area $\theta(t)$ and, correspondingly, the optimal pulse shape $V(t)$ for different values of the relaxation constants

γ_1, γ_2. We also considered different values of the pulse energy E_0 and the pulse curvature R of the control fields. For simplicity we choose the duration of the control interval $T = 1$.
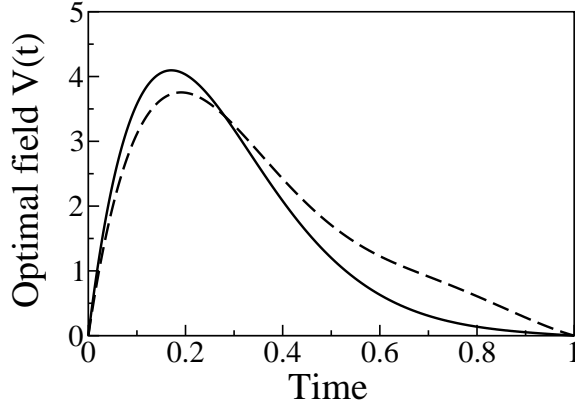

Figure 3.1: The optimal control field $V(t)$ that maximizes the value of n_2 over control
time interval $[0, 1]$ (arbitrary units). Solid line: solution of the Euler-Lagrange
Eq. [3.2] for a system with zero relaxation and dephasing ($\gamma_1 = \gamma_2 = 0$). The
pulse energy is $E_0 = 4.8$ and the pulse curvature $R = 182.2$. Dashed line: optimal
field for a system with non-zero relaxation and dephasing ($\gamma_1 T = 2\gamma_2 T = 0.2$)
with the same pulse energy and curvature $R = 134.32$.

In Fig. [3.1] we show the optimal field $V(t)$ for a two level system without relaxation ($\gamma_1 = \gamma_2 = 0$) and with relaxation ($\gamma_1 T = 2\gamma_2 T = 0.2$) for the same value of the pulse energy E_0. Note, that for both cases the pulse maximum occurs near the beginning of the control interval.

This leads to a rapid increase of the population $\rho_{22}(t)$ and therefore to a maximization of a time averaged occupation n_2. We find that the optimal pulse obtained for the system with relaxation improves the value of n_2 by 50% with respect to a Gaussian pulse and by 25% compared to a square pulse of the same energy. For the case of a system without relaxation the pulse vanishes when the population inversion has been achieved, whereas for a system with relaxation the optimal pulse seems to be broader. One can suggest a simple interpretation of this result. Using Eq. [2.16] we can estimate that in the presence of external field the occupation of the upper level $\rho_{22}(t)$ decays exponentially with the rate $(\gamma_1 + \gamma_2)/2 = 3\gamma_1/4$ that is slower than free decay of the system with the rate γ_1. Therefore, relaxation effects can be partially compensated by a longer application of the field during control interval.

In Fig.[3.2] we show the corresponding dynamics of the population of the excited level $\rho_{22}(t)$ for both cases. As it was mentioned before, the
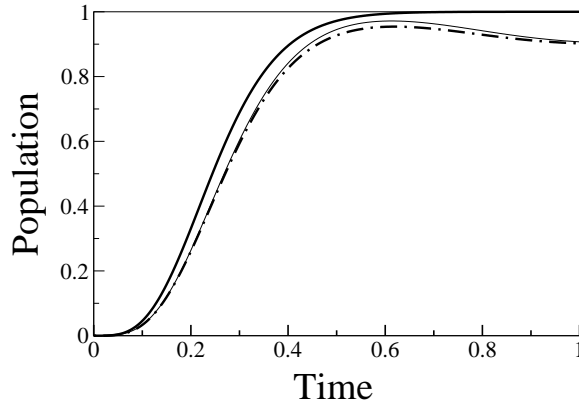
Figure 3.2: Dynamics of the population $\rho_{22}(t)$ corresponding to the fields shown in Fig [3.1] for a system with zero relaxation (thick solid line), and with non-zero relaxation and dephasing (dash dotted line using the approximate formula given by Eq. [2.16], thin solid line-numerical solution of the Liouville equation Eq. [2.13]).
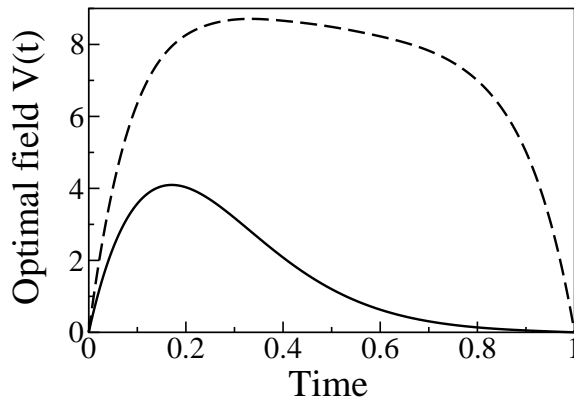

Figure 3.3: The optimal control field $V(t)$ for a two level system with zero relaxation and dephasing ($\gamma_1 = \gamma_2 = 0$, solid line). The pulse energy is $E_0 = 4.57$ and the pulse curvature $R = 128.4$. The dashed line shows the optimal pulse for a system with non-zero relaxation and dephasing ($\gamma_1 T = 2\gamma_2 T = 5$) with the pulse energy $E_0 = 53.54$ and curvature $R = 808.8$.

expression given by Eq. [2.16] is exact for a system without relaxation within the Rotating Wave Approximation. However, for a system with relaxation that Eq. [2.16] also agrees well with the numerical solution of the Liouville equation Eq.[2.13]. This indicates that $V(t)$ fulfills the
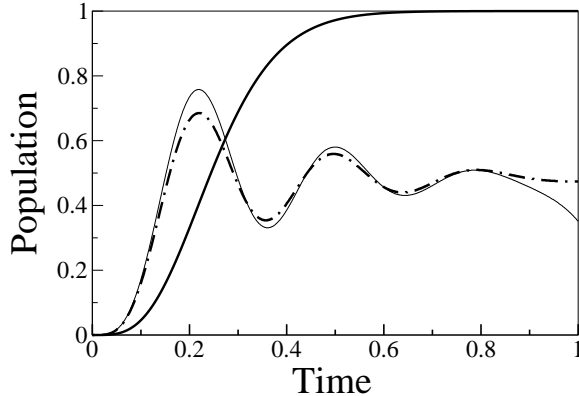
Figure 3.4: Dynamics of the population $\rho_{22}(t)$ for a system with zero relaxation (thick solid line), and with non-zero relaxation and dephasing (dash dotted line-using formula (2.16), thin solid line-numerical solution of the Liouville equation Eq. [2.13]).

condition given by Eq. [2.15] on the control interval [0,T] and therefore our approach is self consistent.

Let us examine now the case of a strong decoherence, for which the controlled system is close to the saturation regime. In Fig. [3.3] we compare the optimal field $V(t)$ for a two level system without relaxation ($\gamma_1 = \gamma_2 = 0$) and with relaxation ($\gamma_1 T = 2\gamma_2 T = 5$). We choose a relatively large pulse energy E_0 of the control pulse in the relaxation regime in order to compensate a rapid decay of the exited level. Indeed, in this case control is not coherent within all control interval. Since the optimal pulse amplitude does not change significantly over time interval, one can conclude that in the strong relaxation regime a pulse with a constant envelope $V(t)$ will be a good approximation for the optimal one.

In Fig. [3.4] we show the corresponding dynamics of the population of the excited level $\rho_{22}(t)$. Surprisingly, the analytical expression for $\rho_{22}(t)$ works also well even for relatively large relaxation rates γ_1, γ_2. The explanation of this result is that the analytical expression for ρ_{22} given by Eq. [2.16] becomes exact for a pulse with a constant envelope $V(t) = V_0$. Because the optimal one is almost constant (except at the boundaries) this expression works also well.

We found that the value of the averaged occupation n_2 increases both for a system with and without relaxation monotonously with the energy E_0 of the optimal control field. In order to illustrate this we plot in Fig. [3.5] the averaged occupation n_2 as a function of the energy E_0 and the curvature R of the optimal fields for a system without relaxation ($\gamma_1 = \gamma_2 = 0$). Note, that pulses of fixed shape (for instance Gaussian)

would show an oscillating behavior for increasing energy due to Rabi oscillations [96]. The monotonous increase of the n_2 with E_0 is a feature which characterizes the optimal pulses.
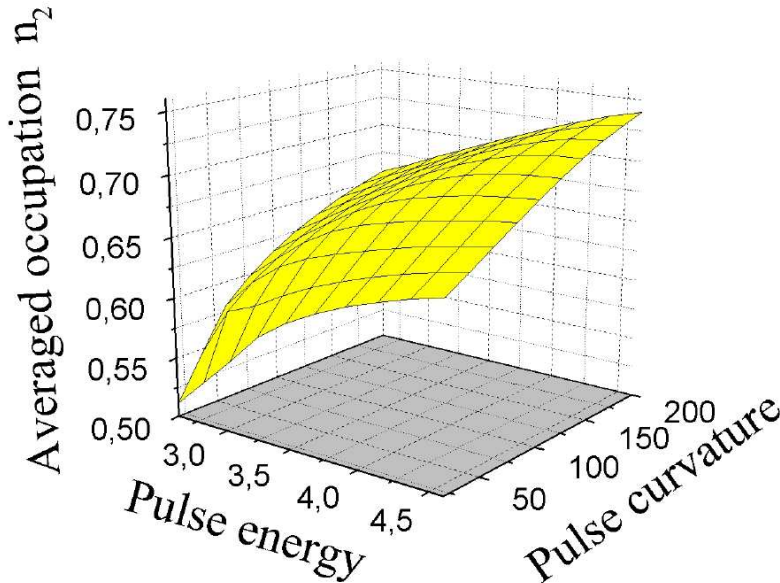

Figure 3.5: Dependence of the averaged occupation n_2 as a function of the pulse energy E_0 and pulse curvature R (see Eq. [2.7]) of the optimal pulses using $\gamma_1 = \gamma_2 = 0$.

3.1.2 Optimal control field calculated using a simplified Lagrangian

In Fig. [3.6] we plot the optimal control field $V(t)$ which maximizes the simplified Lagrangian given by Eq. [2.18] for two level systems with zero ($\gamma_1 = \gamma_2 = 0$) and non-zero ($\gamma_1 T = 2\gamma_2 T = 0.2$) relaxation and dephasing. For the system with zero relaxation and dephasing we use the analytical solution for the optimal control field given by Eq. [2.20]. In both cases the field has its maximum value at $t = 0$ and exhibits a monotonous decay. As in the case of the solutions of the Eq. [2.10] the control field is broader for the system with relaxation in order to compensate decay of the exited state.

In Fig. [3.7] we plot corresponding dynamics of the population $\rho_{22}(t)$. The overall behavior of $\rho_{22}(t)$ is similar to that of the populations shown in Fig. [3.2]. This means that essential physics of the optimal control is already contained in the second order differential equation. The boundary conditions $V(0) = V(T) = 0$ change dramatically the shape of the optimal fields, but they do not affect significantly the dynamics of the controlled
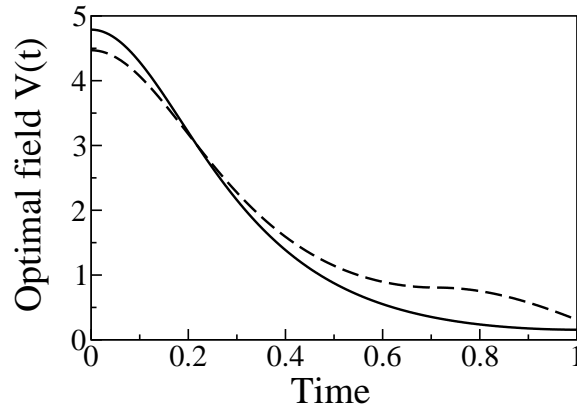
Figure 3.6: The optimal control field $V(t)$ which maximizes the time averaged occupation n_2 in a two level system. Solid line: system with zero relaxation ($\gamma_1 = \gamma_2 = 0$). The pulse energy is $E_0 = 4.6$. The dashed line shows the optimal pulse for the system with non-zero relaxation and dephasing ($\gamma_1 T = 2\gamma_2 T = 0.2$) with the same energy.

system. For a comparison, in Fig. [3.8] we also show results for the case of large relaxation $\gamma_1 T = 2\gamma_2 T = 5$.
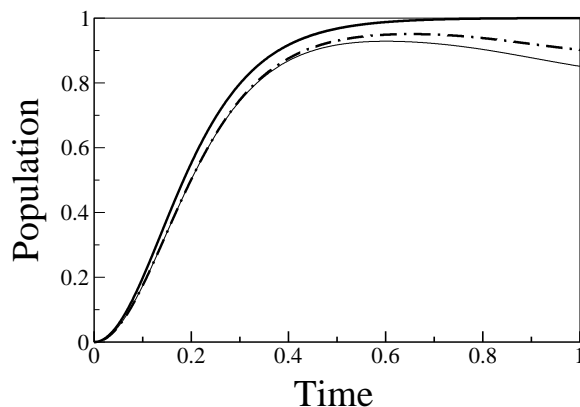

Figure 3.7: Dynamics of the occupation $\rho_{22}(t)$ for system with zero relaxation and dephasing (thick solid line) and non-zero relaxation and dephasing (dash dotted line: approximate analytical solution given by Eq. [2.16], thin solid line: numerical solution of the Liouville equation Eq. [2.13)].

As in Fig. [3.6] the field is maximal at $t = 0$ and exhibits a monotonous decay, and similar to Fig. [3.3] the control field is close to be constant for
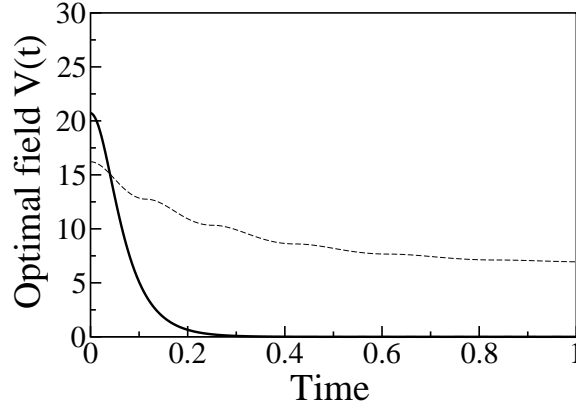
Figure 3.8: The optimal control field $V(t)$ for a two level system with zero relaxation and dephasing ($\gamma_1 = \gamma_2 = 0$, solid line). The pulse energy is $E_0 = 20.50$. Dashed line: optimal field for a system with non-zero relaxation and dephasing ($\gamma_1 T = 2\gamma_2 T = 5$) with the pulse energy $E_0 = 89.72$.

the strong relaxation regime. In Fig. [3.9] we plot the corresponding population $\rho_{22}(t)$ dynamics. As in Fig. [3.4] the system is close to saturation regime.
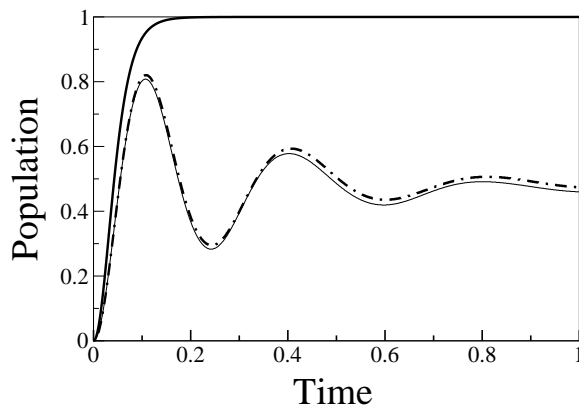

Figure 3.9: Dynamics of the occupation $\rho_{22}(t)$ for system with zero relaxation and dephasing (thick solid line) and with non-zero relaxation and dephasing (dash dotted line using Eq. [2.16], thin solid line-numerical solution of the Liouville equation Eq. [2.13]).

3.2 Application of the QGA to the eigenstate problem for interacting electrons in quantum dots

In this section we present results of the ground and excited states calculations for interacting electrons in a quantum dot using the Quantum Genetic Algorithm.

In the first subsection we perform calculations of the ground state for different simple one and two dimensional systems and compare the obtained results with known analytical solutions. This serves as a good test for the method developed in this work.

In the second subsection we compute the partition function and the excitation spectra of strongly interacting few body systems. With the help of the QGA we investigate the formation of "Wigner molecules" in systems of few confined electrons. We also investigate two different mechanisms for the so called "melting of the Wigner molecule", namely due to thermal and quantum fluctuations.

3.2.1 The ground state problem in one and two dimensions

With the purpose to test our method (GA) we apply it to calculate the ground state wave function $\Psi(x)$ in the case of different external potentials in one and two dimensions. For each iteration of the QGA we evaluate the fitness function for the different individuals of the population: $E_j = E[\psi_j] = < \Psi_j|\hat{H}|\Psi_j >$. Then follow the steps described in the Theory section [2.2]. This process is repeated until the values of the fitness function converge to the minimal value of the energy. In the figures presented below we show the results for the density probability of the ground state and the behavior of the fitness function during the iterative GA-procedure.

Let us start from the ground state problem for one particle captured in the region [0,L] being in the infinite square well. The analytical solution gives the lowest energy state with energy $E = \pi^2/2L^2$ corresponding to the ground state wavefunction

$$\Psi(x) = \sqrt{2/L}\sin(\pi x/L). \tag{3.3}$$

In Fig. [3.10] we show the calculated ground state particle density $|\Psi(x)|^2$ for a potential well with infinite walls at $x = 0$ and $x = 1$ (throughout this chapter we use atomic units). In the inset of the Fig. [3.10] we show the evolution of the mean energy of the population.The mean population energy is defined using calculated energies of all population members. It is clear that the QGA converges rapidly to the ground state. The

ground-state energy calculated using our method is very close to the exact value $E = \pi^2/2 = 4.9348...$ up to an error of $10^{-5}\%$ already after 20 iterations. We also performed calculations for other analytically solvable problems, namely the harmonic potential $U(x) = \frac{1}{2}\omega^2(x - 0.5)^2$. In this
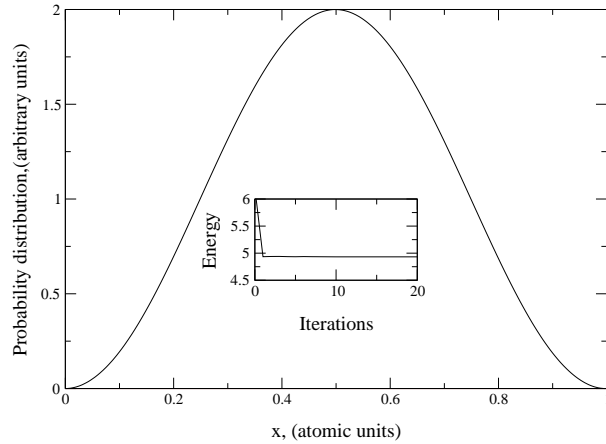

Figure 3.10: Ground state spatial density distribution of an electron $|\Psi(x)|^2$ in a one-dimensional infinite well (defined on the interval [0,1]) calculated using the QGA. Inset figure: evolution of the fitness as a function of the number of iterations.

case the ground state energy is $E = \omega/2$, and the ground state wavefunction is given by

$$\Psi(x) = \left(\omega/\pi\right)^{1/4} \exp(-\omega(x - 0.5)^2/2). \tag{3.4}$$

In Fig. [3.11] the calculated ground density state is shown for $\omega = 2\sqrt{10} \cdot 10^2$. The value of the ω is chosen rather large, therefore one can neglect the influence of the walls on the final result. In the inset of Fig. [3.11] we show the evolution of the mean energy of the population. It converges slower than in the case of the infinite well because the QGA should find rather localized solution. However, it converges after only 30 iterations. For the ground-state energy the QGA yields $E^{QGA} = 316.29$, while the analytical result is $E = 316.22$ which represents a discrepancy of less than 0.02% after 30 iterations.

In order to check whether the QGA finds a solution in more complicated cases, if, for example, the spatial distribution of the electron density has not one but two maxima, we performed calculations for the case of anharmonic potential with two distinct minima.

In Fig. [3.12] we present the calculated ground state density for an anharmonic potential of the form

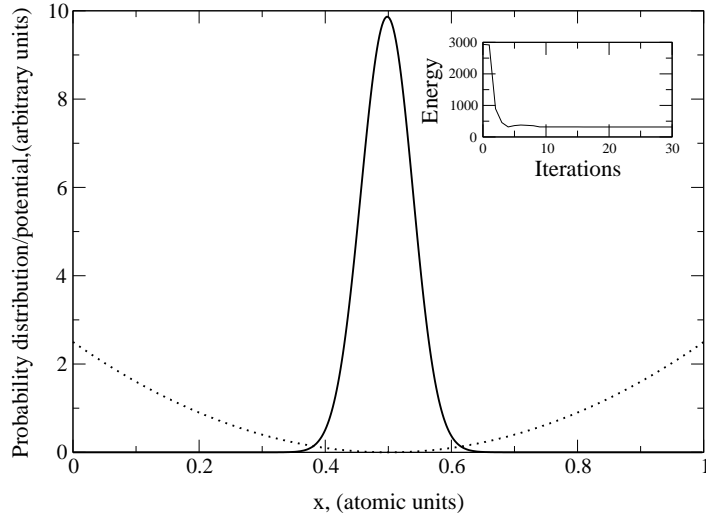$$U(x) = k_0 - k_2 x^2 + k_3 x^3 + k_4 x^4, \tag{3.5}$$

64

Figure 3.11: Calculated spatial distribution of electron density $|\Psi(x)|^2$ (solid line)
for an electron in a 1D harmonic potential (dotted line). The inset shows the
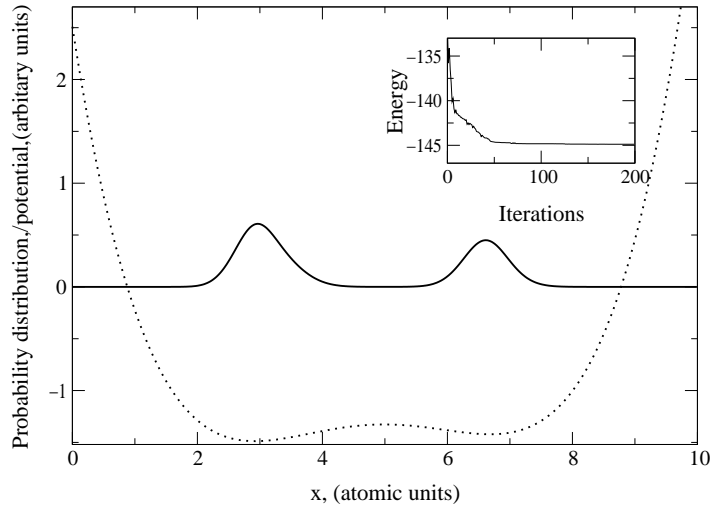evolution of the fitness as a function of the number of iterations.

Figure 3.12: Calculated spatial distribution of the electron density $|\Psi(x)|^2$ (solid line)
for an electron in an anharmonic potential of the forth order (dotted line). The
inset shows the evolution of the fitness as a function of the number of iterations.

with $k_0 = -137.7074997$, $k_2 = 7$, $k_3 = 0.5$, and $k_4 = 1$. We use these
values of the parameters in order to compare with existing calculations
performed using the spectral method [81]. In the inset of Fig. [3.12] we
also show the evolution of the mean energy of the population. It con-
verges slower than in the previous two cases. The reason is that the QGA
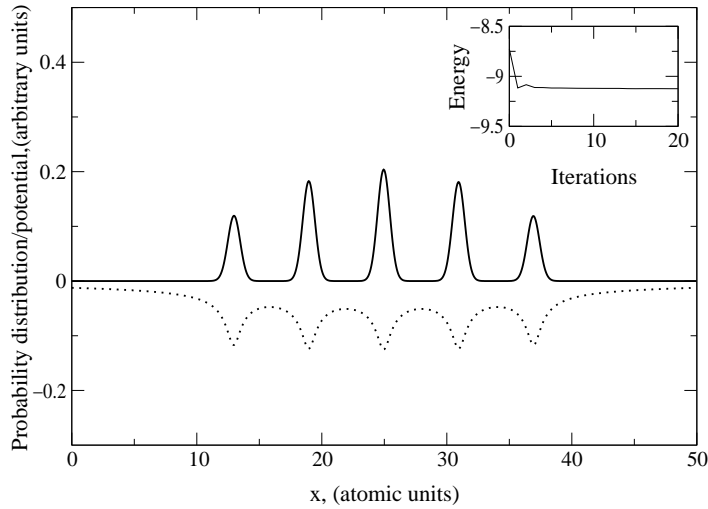operates is more complicated space of possible solutions. Nevertheless,

Figure 3.13: Calculated spatial distribution of the electron density $|\Psi(x)|^2$ (solid line) for an electron in a potential produced by a chain of positive ions (dotted line). The inset shows the convergence behavior of the fitness function.

algorithm converges after 200 iterations. Our calculated ground-state energy is $E^{QGA} = -144.87$, whereas the value obtained by using the spectral method is $E = -144.96$, i.e., the discrepancy is less than 0.06% after 200 iterations.

Our next example deals with the ground state of an electron subject to a 1D potential produced by a chain of 5 positive charged ions, which is given by

$$U(x) = \sum_{i=1}^{5} \frac{Q}{\sqrt{(x - x_i)^2 + S}}, \tag{3.6}$$

where Q is the charge of each ion and x_i its position. S is a cutoff parameter. This smooth 1D ionic potential has been used, for instance, in the context of the Coulomb explosion of small clusters induced by intense femtosecond laser pulses [28, 107]. In the QGA-calculations for this potential, and in order to speed up the convergence process, we use for the initial populations trial functions of the form

$$\Psi_j(x) = \sum_{j=1}^{5} A_j \, \exp(-(x - x_j)^2/\sigma_j^2)(x - a)(b - x), \tag{3.7}$$

having 5 peaks, where the amplitudes A_j, widths $0 < \sigma_j < b - a$ and peak positions $x_j \in (a, b)$ are random numbers. In our calculations we have used $Q = 5, a = 0, b = 50$, $x_i = 13, 19, 25, 31, 37$, and $S = 0.25$. Note, that the calculated probability distribution, shown in Fig. [3.13], has the same symmetry properties as the external potential $U(x)$. In the inset of
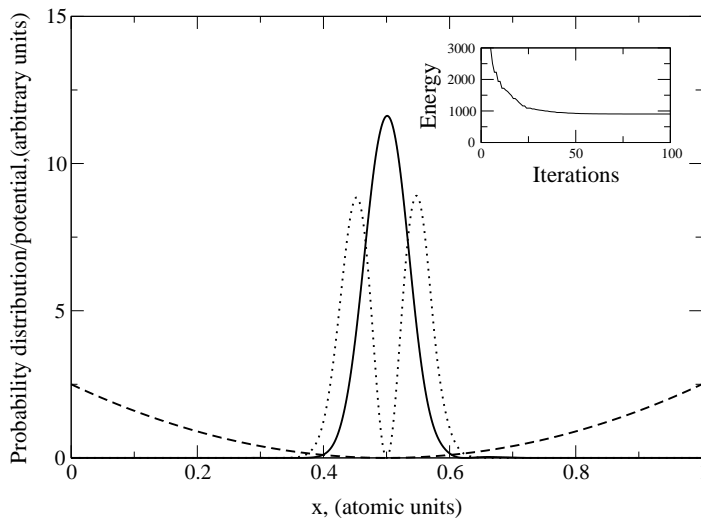
Figure 3.14: Calculated densities $|\phi_1(x)|^2$ (solid line) and $|\phi_2(x)|^2$ (dotted line) of two orbitals which build the first triplet-state wave function for two noninteracting electrons in a 1D harmonic potential (dashed line). The convergence behavior of the fitness function is shown in the inset.

Fig. [3.13] we plot the evolution of energy of the best "offspring" in the population. It is clear that using appropriate initial guess for the form of the wave function can considerably accelerate the convergence of the QGA. In this example the genetic process converges after only 20 iterations.

Now we study the simplest case of the few body problem. For simplicity we consider first a system of two noninteracting fermions trapped into harmonic potential $V(x) = \frac{1}{2}\omega^2(x - 0.5)^2$. We assume that the wavefunction of electrons has symmetric spin part, and therefore we search for the antisymmetric spatial solutions. The triplet-state wave function of two noninteracting electrons having the lowest energy can be written as $\Psi(x, x') = [\phi_1(x)\phi_2(x') - \phi_2(x)\phi_1(x')]/\sqrt{2}$, where $\phi_1(x)$ and $\phi_2(x)$ are the ground-state and first excited state of the single-particle Hamiltonian, respectively.

With the help of the QGA we have determined $\phi_1(x)$ and $\phi_2(x)$, and consequently $\Psi(x, x')$ for the harmonic potential described above. For this calculations the individuals of the successive populations were the pairs $\{\phi_1(x), \phi_2(x)\}$.

In Fig. [3.14] the functions $\phi_1^2(x)$ and $\phi_2^2(x)$ for this case are shown using $\omega = \sqrt{20} \cdot 10^2$. Note, that this procedure yields both the two-particle triplet state with the lowest energy and first two single-particle states of the single particle Hamiltonian. For the ground-state energy the QGA yields $E^{QGA} = 894.90$, while the analytical result is $E = 2\omega = 894.43$.

Let us now test the QGA by determining the ground state wavefunction in two dimensions under different external potentials.
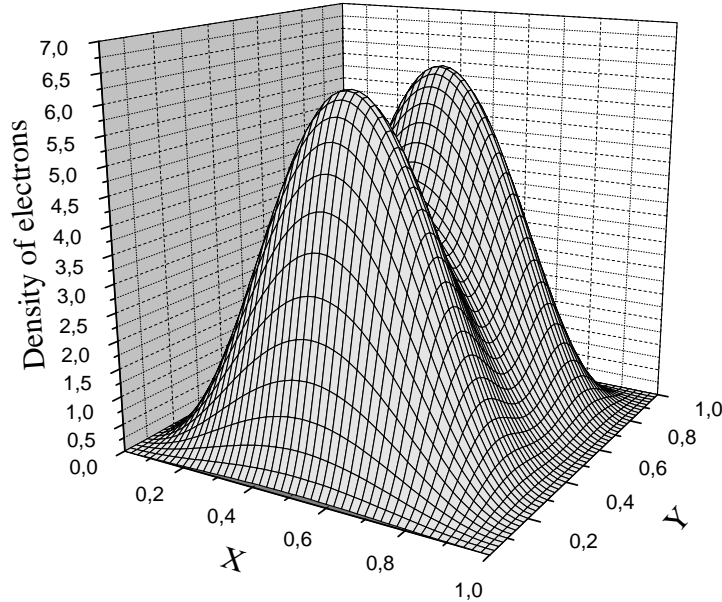
67

Figure 3.15: Density distribution $\rho_{QGA}(x, y)$ for the ground state of two noninter-acting fermionic particles (triplet state) in a square infinite well.

The region of discretization Ω is chosen as follows. For practical pur-poses we consider a rectangular box $\Omega \equiv \{(x, y), 0 \leq x \leq d, 0 \leq y \leq d\}$ in two dimensions. The value of the length d is 1 atomic unit. We also assume that the external potential outside Ω is infinitely high. In all 2D examples presented here we use a lattice with 100 by 100 grid points. To calculate the kinetic energy term in the Hamiltonian given by Eq. [2.29] we use a high-order finite-difference formula [83].

In our first example we perform the evaluation of the ground state for two noninteracting particles (in a triplet state) confined into the infinite well.

The ground state of this system is degenerate, and the wave functions corresponding to the different degenerated states are antisymmetric. One possible solution is given by

$$
\begin{aligned}
\Psi(x_1, y_1, x_2, y_2) \quad = \quad & 4[\sin(\pi x_1)\sin(\pi y_1)\sin(2\pi x_2)\sin(\pi y_2) \\
& - \sin(\pi x_2)\sin(\pi y_2)\sin(2\pi x_1)\sin(\pi y_1)]. \quad (3.8)
\end{aligned}
$$

The QGA procedure converges rapidly to a solution having the same sym-metry of the function given by Eq. (3.8). In Fig. [3.15] we show the
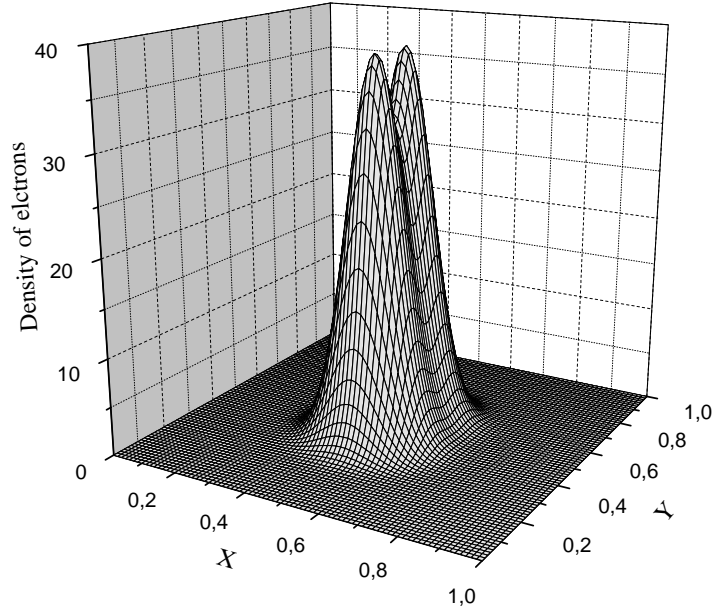
Figure 3.16: Density distribution $\rho_{QGA}(x,y)$ for the ground state of two noninteracting fermionic particles (triplet state) in an external harmonic potential.

ground state spatial density $\rho_{QGA}(\vec{r}) = \int |\Psi_{QGA}(\vec{r}, \vec{r'})|^2 d\vec{r'}$ obtained from the QGA. The overall shape of the solution and its symmetry are in good agreement with the exact result. The calculated value of the ground energy (E^{QGA}=34.543619) is also in a very good agreement with the analytical result ($E = 7\pi^2/2$=34.543615), the relative error being less than $10^{-5}\%$.

In the next example we determine the ground state of two noninteracting particles (in a triplet state) in a 2D harmonic potential described by potential

$$U(x,y) = \frac{1}{2}\omega^2((x-0.5)^2 + (y-0.5)^2), \qquad (3.9)$$

using $\omega = 10^2$. The analytical solution for one of the degenerate triplet state reads

$$\Psi(x_1, y_1, x_2, y_2) = \frac{\omega^{\frac{3}{2}}}{\pi} \exp\{-\omega(x_1^2 + y_1^2)/2\} \exp\{-\omega(x_2^2 + y_2^2)/2\}(x_2 - x_1).$$
$$(3.10)$$

In Fig. [3.16] we present the ground state density $\rho_{QGA}(x,y)$ for this problem. In this case there is also good agreement between the result obtained

from the QGA and the exact result. The calculated value of the ground-state energy is $E^{QGA} = 300.0024$, which compares well with the exact one ($E = 3\omega = 300$).

3.2.2 Formation of a "Wigner molecule" and its "melting"

The fact that for noninteracting quantum problems the QGA yields good convergence to the exact results motivated us to apply our approach to test its efficiency for interacting systems. Therefore, we study two interacting particles (in a triplet state) in 1D using an artificially smoothed Coulomb-like interacting potential

$$V(x_1, x_2) = \frac{Q}{\sqrt{(x_1 - x_2)^2 + \varepsilon_s^2}}, \qquad (3.11)$$

where ε_s is a smoothing coefficient. Q is the strength of the interparticle interaction. In our calculations we use $\varepsilon_s = \sqrt{3}$. As we mentioned above we seek for the Hartree-Fock approximation. Therefore, we construct an initial population $\{\Psi_i(x_1, x_2)\}$ consisting of antisymmetric functions of the form $\Psi(x_1, x_2) = [\psi_1(x_1)\psi_2(x_2) - \psi_2(x_1)\psi_1(x_2)]$ for particles in a triplet state. After convergence of the QGA we determine the spatial density of the particles given by $\rho_{QGA}(x) = \int |\Psi_{QGA}(x, x')|^2 dx'$.
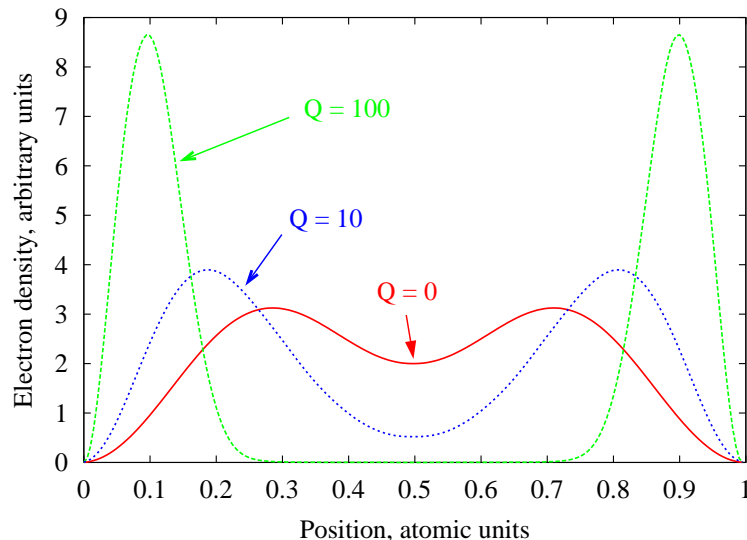

Figure 3.17: Density distribution $\rho_{QGA}(x)$ for two interacting fermionic particles in a triplet state in one-dimensional infinite well. The different curves refer to different strengths Q of the interaction $V(x_1, x_2) = Q/\sqrt{(x_1 - x_2)^2 + 3}$ between the particles.

70

In Fig. [3.17] we show the calculated $\rho_{QGA}(x)$ corresponding to the Hartree-Fock approximation to the ground state for different values of the interaction strength Q. For $Q = 0$ (noninteracting case) the solution is
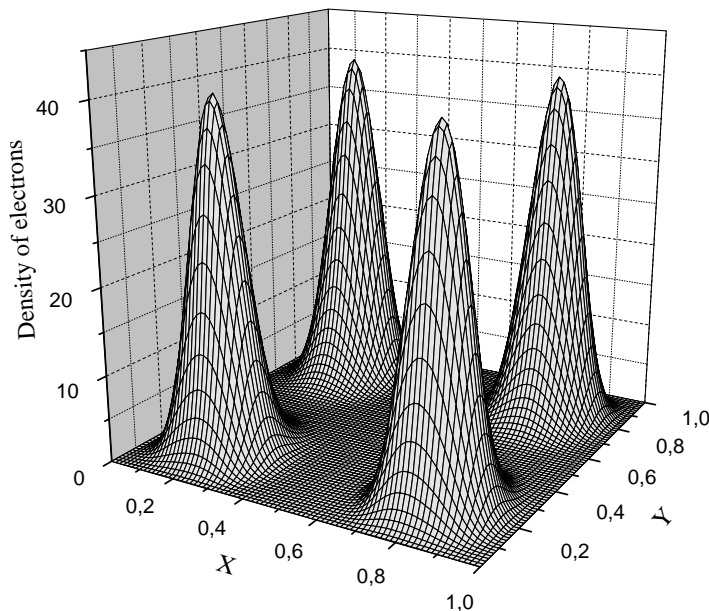

Figure 3.18: Electron density distribution $\rho_{QGA}(x, y)$ of two interacting electrons in a triplet state in a square infinite well in the low density limit (large box size). The spatial coordinates are rescaled to unity. Note the localization of the electron density that corresponds to formation of the so-called "Wigner molecule".

built up from the ground state and the first excited state of the single particle problem. As a consequence, the particles are well delocalized and minimize the kinetic energy.

In contrast, in the interacting case the repulsive term of the Hamiltonian forces the particles to be far away from each other. This effect increases with increasing interaction strength, and leads to a localization near the opposite walls. For $Q = 100$ the overlap between one particle wavefunctions becomes negligible.

Now let us study the ground state of two particles strongly interacting via repulsive Coulomb potential in 2D. This is a common problem in the physics of quantum dots [86, 74, 75, 87]. In this case the repulsive interaction potential is given by

$$U(\vec{r}_1, \vec{r}_2) = \frac{e^2}{|\vec{r}_1 - \vec{r}_2|}. \tag{3.12}$$

For this example we rescale the size of the box by setting $d = 1000$. This corresponds to the low-density case. In Fig. [3.18] we show the calculated density distribution $\rho_{QGA}(x, y)$. For low electronic densities, the contribution of the Coulomb interaction is more important than the contribution of the kinetic energy of the particles. This leads to a strong localization of the particles in opposite corners of the square box, which minimizes the energy of the system. This effect may correspond to the well known Wigner crystallization [84]. Note that for the two-particle 1D system discussed above this effect also takes place upon increase of the interaction strength Q (see Fig. [3.17]). The Wigner crystallization in quantum dots, which is also described as formation of a "Wigner molecule", has been obtained recently using other theoretical approaches [74, 82, 87]. In fact, our calculated density shown in Fig. [3.18] is in good agreement with other methods [74]. This is a remarkable result.
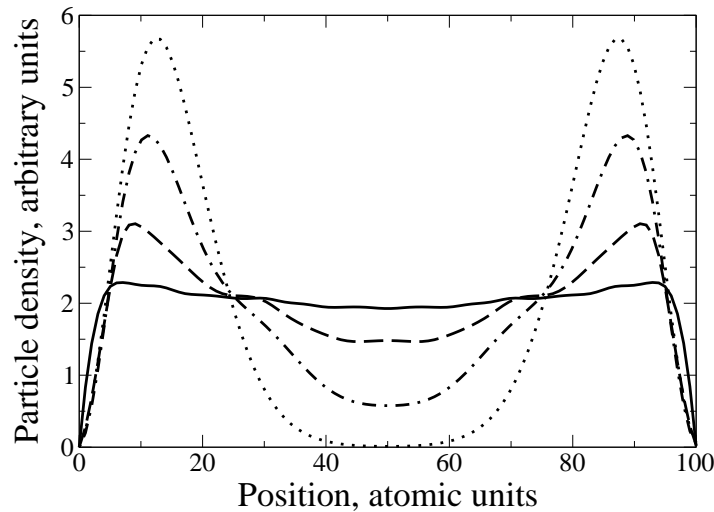

Figure 3.19: Particle density $\rho(x)$ of two interacting particles in an infinite well with the width $L = 100$, using $\beta = 4 \cdot 10^7$ (dotted line),$2 \cdot 10^6$ (dash-dotted line),$1 \cdot 10^6$ (dashed line),$1 \cdot 10^5$ (solid line).

Next, we present results of calculations of the partition function together with the excitation spectrum. Once calculated, the excitation spectrum can be used to derive any kind of quantum statistical values. For instance, with a help of partition function we compute particle densities for different temperatures.

We consider particles in a triplet state being in the 1D infinite well with the width L and interacting via repulsive Coulomb potential. In

order to eliminate logarithmic singularity which is typical for Coulomb interaction in one dimension [28], we use a smoothed interaction potential given by Eq. [3.11]. In these calculations we use $L = 100$ that guarantees low electron density and set $\varepsilon_s = 1/\sqrt{10}$.

In his pioneering work [84], Wigner pointed out that the electron gas would crystallize at sufficiently low temperature and density. When thermal fluctuations (in energy units) becomes comparable with the energy of the interparticle interaction, the opposite to the Wigner crystallization transition occurs, i.e. melting of the Wigner crystal.

First we present the results of our calculations of the melting of a "Wigner molecule" in one dimension due to increasing of thermal fluctuations. In Fig. [3.19] we show the electron density for the case of two particle system. In our calculations we set parameter $\beta = 4 \cdot 10^7, 2 \cdot 10^6, 1 \cdot 10^6, 1 \cdot 10^5$ and we choose size of the well $a = 100$. The density of particles $\rho(x)$ clearly becomes more delocalized with increasing of the temperature (decreasing of the parameter β) and for $\beta = 1 \cdot 10^5$ it is almost uniform.

In Fig. [3.20] we plot the particle density for three particles with parallel spins, using parameter $\beta = 6 \cdot 10^7, 3 \cdot 10^6, 1.5 \cdot 10^6, 1.5 \cdot 10^5$ and for the same size of the well. As in Fig. [3.19], initially localized particle density is smeared out with increasing of the temperature. Because of the small amount of the particles in the system, this transition is quite smooth.
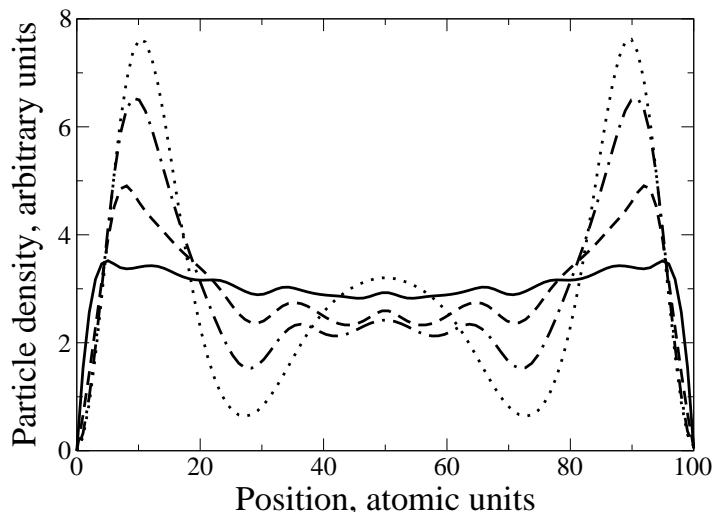

Figure 3.20: Particle density $\rho(x)$ of three interacting particles in an infinite well with the width $L = 100$, using $\beta = 6 \cdot 10^7$ (dotted line), $3 \cdot 10^6$ (dash-dotted line), $1.5 \cdot 10^6$ (dashed line), $1.5 \cdot 10^5$ (solid line).

Now let us investigate the behavior of the finite quantum system at low temperatures, i.e., in the quantum regime. In contrast to classical systems, recently a new "Wigner molecule melting" scenario which is caused by quantum fluctuations and exists even at zero temperature [90] has been studied. It was shown, that delocalization of the electron density occurs when the ratio of the kinetic energy to the Coulomb energy exceeds a certain threshold [90]. The kinetic energy E_{kin} of a quantum system with fixed number of particles and variable size L scales as $E_{kin} \sim L^{-2}$, while the Coulomb energy E_C scales only as $E_C \sim L^{-1}$. Therefore, with decreasing of the size of the system quantum fluctuations become more and more significant (due to the Heisenberg's uncertainty principle) and quantum phase transition would occur. In Fig. [3.21] we present results
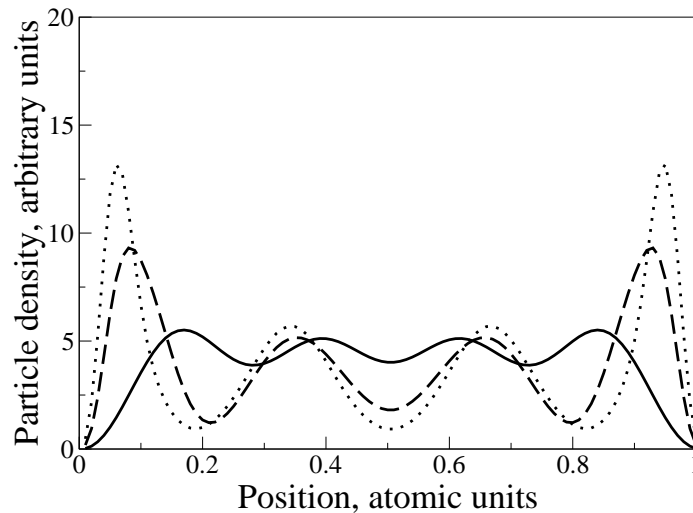

Figure 3.21: Rescaled particle density $\rho(x)$ of four interacting particles in an infinite well at zero temperature using width of the well $L = 500$ (dotted line), $L = 100$ (dashed line), $L = 1$ (solid line).

for the calculation of the particle density $\rho(x)$ for different sizes of the well $a = 500, 100, 1$ at zero temperature. In order to visualize these results we re-scale calculated $\rho(x)$ on the interval [0,1]. From Fig. [3.21] it becomes clear, that with decreasing of the size of the system electron density tends to be more delocalized, i.e. a kind of "Wigner molecule melting" takes place in the system.

3.3 Optimal field for control of the photon assisted tunneling between quantum dots

In this section we present results of our studies on optimal control in nanostructures in the presence of decoherence. Using the genetic algorithm we perform a search for the optimal shape of the control field in order to maximize the transferred charge in the double quantum dot system.

3.3.1 Numerical solution using the genetic algorithm: the influence of relaxation on the optimal control

The parameters used in our calculations are given in terms of the tunneling matrix element d. The energy difference $\Delta \varepsilon = \varepsilon_2 - \varepsilon_1$ must be much larger than d to ensure that the ground state of the double quantum dot is localized on the left side and the excited state is localized on the right side. This also leads to a sharper resonance behavior. Therefore we set $\Delta \varepsilon = 24d$.

In our calculations we use symmetric coupling of the QD to the reservoirs $\Gamma_1 = \Gamma_2 \equiv \Gamma$ and compute optimal field shape for different values of the coupling constants $\Gamma = 0, 0.01d, 0.05d$. It is important to point out that Γ must be smaller than d, so that the Rabi oscillations do not become overdamped. If Γ is large the system saturates very rapidly to $\rho_{11} = \rho_{22} = 1/2$ and no interesting transient dynamics can be observed. Finally, we choose the control interval $T = 100\hbar/d$ which is large enough to allow back and forth motion of the electrons between the quantum dots. Typically T is the same order of magnitude as $\hbar/\Gamma$.

In our calculations we also put a constraint on the minimal width of the pulse in order to describe pulses which can be achieved experimentally. In our calculations this minimal width is naturally determined by the discretization of the time interval and by the smoothness parameters k_c and k_m of the crossover and mutation operations (see Eqs. [2.33,2.34]).

We discuss first results for $U = 0$, i.e., neglecting the interdot Coulomb repulsion. The search for the optimal pulse in the system described in the Theory section 2.3 is a difficult task. From the elementary analysis of Eq. [2.43] it is clear that the optimal pulse should first be able to transfer an electron from left to the right QD (inversion of the occupation) and then to keep this situation as long as possible. However, there are many different pulse shapes able to achieve this situation and it is *a priori* not clear which one maximizes the transferred charge Q_T.

For $\Gamma = 0$, for example, the system given by Eq. [2.43] can be solved analytically for some limiting cases. If, for example, the external field is periodic in time, $V(t) = V_0 \cos \omega t$, with a constant amplitude V_0, an
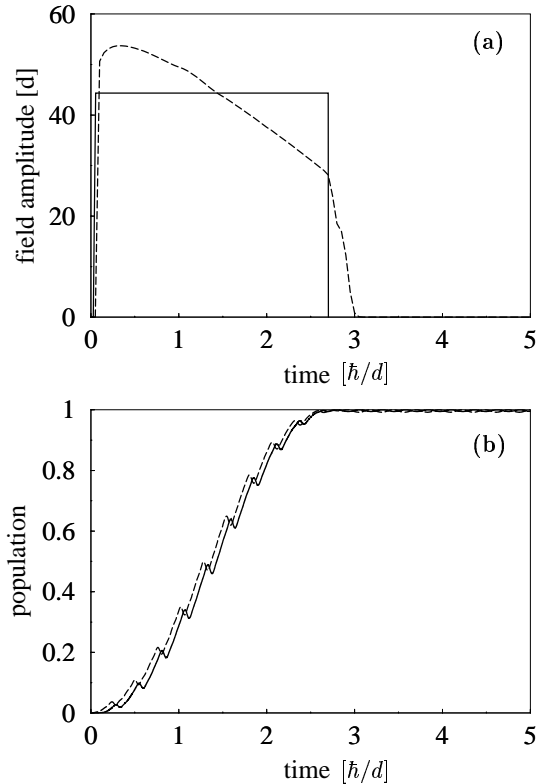
Figure 3.22: Optimal control field for the isolated double quantum dot ($\Gamma = 0$). (a) Solid line: reference square pulse of duration $\tau = \pi\Omega_{max}^{-1}$ and intensity V_0 yielding the first maximum of $\mathrm{J}_1(V_0/\hbar\omega)$ (see text), and having energy E_0. Dashed line: optimal pulse shape for the maximization of the charge transferred from the left to the right quantum dot. The pulse energy is E_0. (b) Corresponding time-dependence of the occupation $\rho_{22}(t)$ on the second dot for the pulses shown in (a).

electron placed on one of the dots will oscillate back and forth between the dots with the Rabi frequency $\Omega = 2d/\hbar \; \mathrm{J}_1(V_0/\hbar\omega)$ [98, 99], J_1 being the Bessel function of order 1, if the system absorbs one photon. The carrier frequency ω must fulfill the resonance condition $\hbar\omega = \sqrt{\Delta\varepsilon^2 + 4d^2}$. The description of the tunneling dynamics for pulses of varying intensity is much more complicated, because the Rabi frequency changes in time.

Thus, for pulses of constant amplitude there is an upper limit Ω_{max} for the Rabi frequency which is obtained when the ratio $x = V_0/\hbar\omega$ is such that the function $\mathrm{J}_1(x)$ has its first maximum. Using this property we construct a reference pulse of square shape ($V(t) = V_0$ for $0 \leq t \leq \tau$ and $V(t) = 0$ otherwise) with intensity V_0 as defined above and duration $\tau = \pi\Omega_{max}^{-1}$. In the following we will use the energy E_0 of such reference pulse as a unit of pulse energies. In principle one would expect that the reference pulse defined above exactly achieves an inversion of the occupation in the double quantum dot within the shortest time (assuming only one-photon absorption). However, as we show below, such a pulse shape is not the
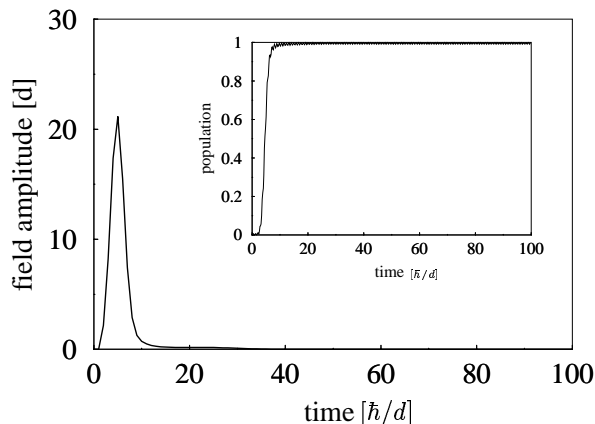
Figure 3.23: Optimal pulse shape for the maximization of the charge transferred from the left to the right quantum dot. The pulse energy is $E = 0.57E_0$ and the coupling to the reservoirs is chosen to be $\Gamma = 10^{-6}d$. Inset: corresponding time-dependence of the occupation $\rho_{22}(t)$ of the right quantum dot.

optimal one.

In Fig. [3.22] we compare the effect that is induced on the isolated double quantum dot ($\Gamma = 0$) by the reference square pulse with that induced by the optimal one calculated using the GA and having the same energy E_0. As one can see in Fig. [3.22(b)],the GA finds a pulse shape which induces a slightly faster transfer of the charge. This result inspired us to perform calculations for more complicated problems. In the following examples we are searching also for the minimal pulse energy E.

In Fig. [3.23] we show the optimized pulse shape for the maximization of the charge transfer in the almost isolated double quantum dot ($\Gamma = 10^{-6}$). The optimal pulse excites the system at the beginning of the control time interval inducing an inversion of the occupation. $\rho_{22}(t)$ reaches the value 1 when the pulse goes to zero. Since Γ is very small, this occupation remains constant in time. As a consequence the transferred charge Q_T is maximized. From the comparison between Figs. [3.22] and [3.23] we see that a limitation of the minimal pulse width, that we employed for this calculations, leads to more symmetric and smooth optimal solutions. The corresponding evolution of the occupation of the second quantum dot is shown in the inset of Fig. [3.23].

In Fig. [3.24] we show the optimal field envelope and the induced occupation $\rho_{22}(t)$ dynamics in the case of the weak coupling to reservoirs with coupling constant $\Gamma = 0.01d$. Note that the optimal field is structured as a sequence of two pulses (see Fig. [3.24(a)]). The first one acts at the beginning and has the proper shape to bring the occupation of the second QD to a value close to 1. However, since $\Gamma \neq 0$ (according to Eqs. [2.43]) $\rho_{22}(t)$
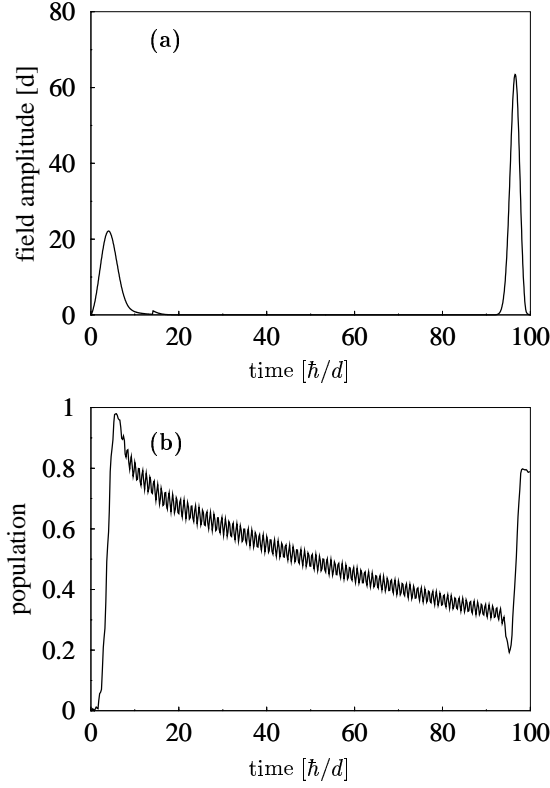
Figure 3.24: (a) Optimal pulse shape which induces maximal current using $\Gamma = 0.01d$. The pulse energy is $E = 4.26E_0$. (b) Corresponding behavior of $\rho_{22}(t)$.

starts to decrease as soon as the first pulse goes to zero. Shortly before the end of the control time interval the second pulse brings the occupation $\rho_{22}(t)$ again to a high value (Fig. [3.24(b)]). The structure of the optimal pulse can be easily interpreted with the help of the expression of Q_T as a functional of $\rho_{22}(t)$ (see Eq. [2.46]). The first pulse tends to keep the term $\frac{e\,\Gamma_2}{\hbar} \int_0^T dt\, \rho_{22}(t)$ as large as possible, whereas the second pulse acts to increase $e\rho_{22}(T)$. As a consequence, Q_T is maximized. Fig. [3.25] shows results for the same system, but with larger coupling constant, namely $\Gamma = 0.05d$. As can be seen in Fig. [3.25(a)], in this case the optimal solution also exhibits pulses at the beginning and at the end of the control interval, but also a complicated sequence of pulses between them which prevent $\rho_{22}(t)$ to go to zero. ρ_{22} is stabilized around the value $1/2$, i.e. at the state where both dots are equally occupied (see Fig. [3.25(b)]).

If the coupling constant Γ is further increased, the structure in the middle of the time interval becomes more important. In the limit of large Γ we expect a square pulse to maximize Q_T, since the system goes into the saturation regime and in this case the pulse only needs to transfer charge
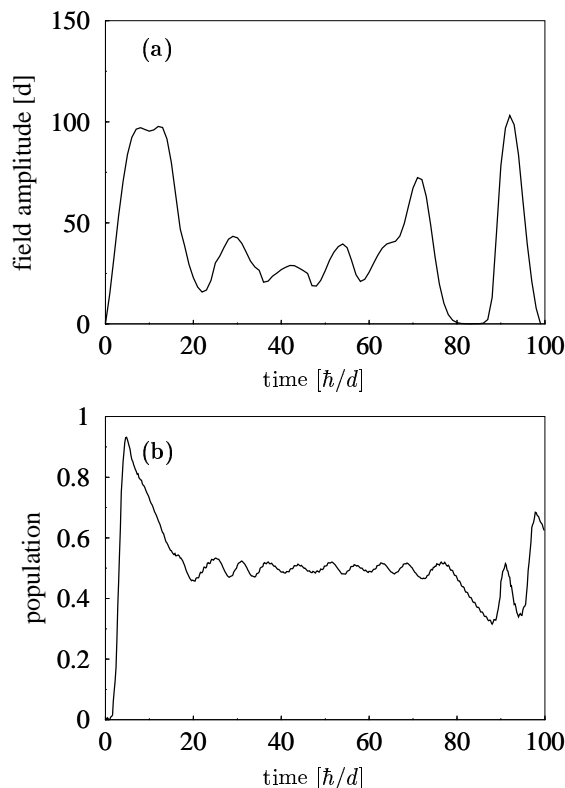
Figure 3.25: (a) Optimal pulse shape using $\Gamma = 0.05d$. The pulse energy is $E = 121E_0$. (b) Corresponding time-dependence of the occupation $\rho_{22}(t)$.

at some constant rate with a value of the order of Γ.

In order to illustrate the progress achieved by the genetic algorithm during the optimization process we show (for the case of $\Gamma = 0.05d$) in Fig. [3.26] the shape (envelope) of the fittest pulse at the different stages of the genetic evolution, . In Fig. [3.26] (1st iteration) one of the pulses of the initial population (parents) is plotted. As all other parents this pulse is a Gaussian-like. The best representative, shown in Fig. [3.26], induces an excitation of the system at the early beginning of the control time interval. The successive application of the genetic operations improves the pulse shape and transforms the initial Gaussians in more complicated pulse sequences. As a result, the envelope of the fittest pulse of the 10th generation Fig. [3.26], for instance, exhibits several peaks. After 30 iterations the pulse form already exhibits most of the features of the optimal pulse, and after approximately 50 iterations it converges to the optimal one.

To illustrate this convergence we show in Fig. [3.27] the evolution of the transfered charge $Q_T[V(t)]$ for the best pulse as a function of the number of iterations of the GA. It is clear that after already 50 iterations
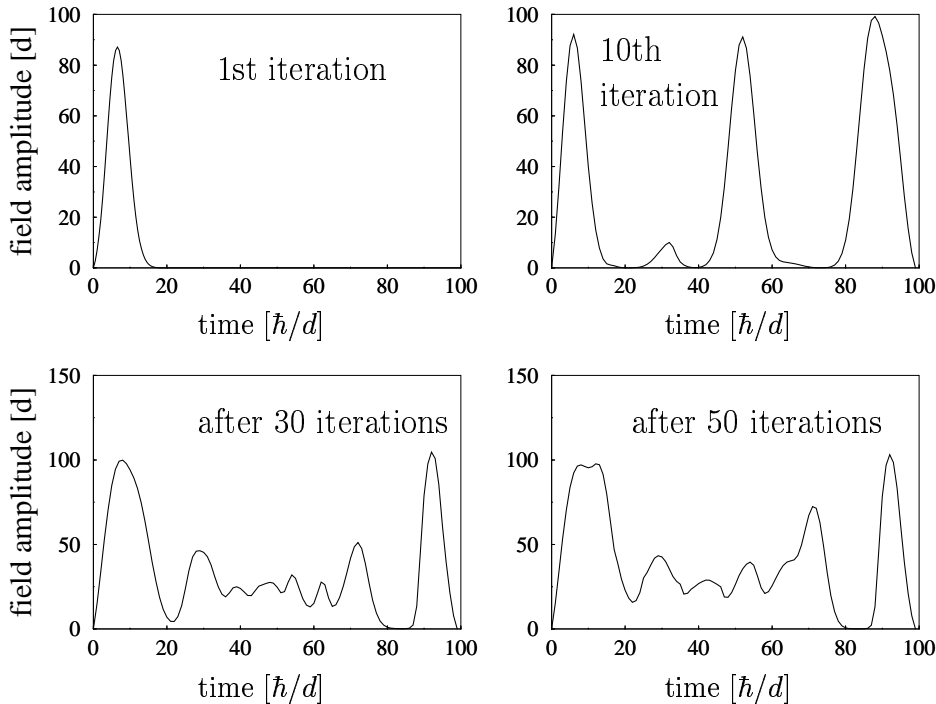
Figure 3.26: Illustration of the optimization process using genetic algorithms. Evolution of the "fittest" pulse shape for maximization of the current using $\Gamma = 0.05d$.

the pulse induces a transferred charge very close to the optimal one. For the sake of comparison in Fig. [3.28] we show the optimal pulse shape which maximizes the mean occupation of the second QD, using as fitness function the time average of the occupation on the second quantum dot, $P_{22} = \int_0^T dt\, \rho_{22}(t)$ (for Γ=0.01d,0.05d). Interestingly, the optimal pulse has also two peak structure. Indeed, the first pulse pumps one electron from the left to the right QD. The reason for the position of the second pulse is that the efficiency to excite the system is maximal when $\rho_{22}(t)$ reaches its minimum, i.e. at the end of the control interval. This result is a direct consequence of the nonlinear character of the considered control problem. One should also mention that the optimal control field has the same properties for larger relaxation in the system, namely some sequence of pulses not only at the beginning and at the and of the control interval, but also some in between.

From this example one can learn that this is a general property of the control fields for open systems. This property one finds for various functionals which one wants to optimize.

In order to investigate the influence of the interdot Coulomb repulsion U we perform calculations similar to those described above, but for the
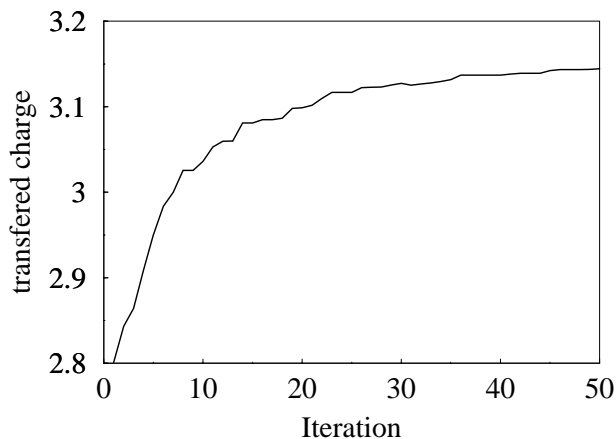
Figure 3.27: Evolution of the transfered charge Q_T for increasing number of iteration of the GA using $\Gamma = 0.05d$.
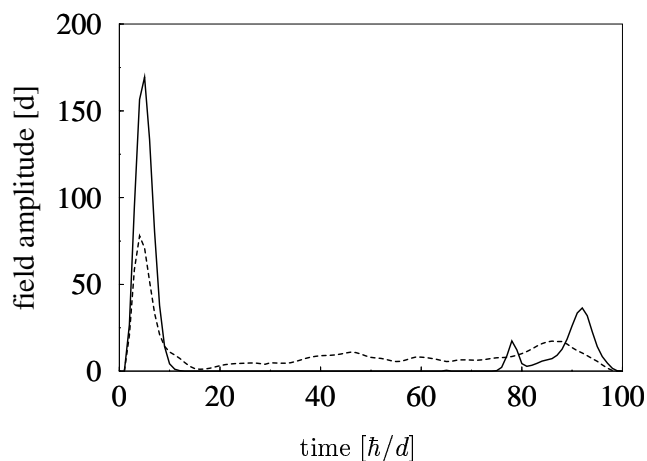

Figure 3.28: Optimized pulse shape using $\Gamma = 0.01d$ (solid line, the pulse energy is $E = 48.4E_0$), and using $\Gamma = 0.05d$ (dashed line, the pulse energy is $E = 13E_0$) for the maximization of the average occupation $P_{22} = \int_0^T dt\, \rho_{22}(t)$ of the second quantum dot (see text).

case $U \rightarrow \infty$ using the same set of coupling parameters Γ. We found that the repulsion between QD leads to a relatively smaller net transferred charge (see Fig. [3.29]). This is due to the fact that $U \rightarrow \infty$ prevents double occupancy in the system. Therefore, an electron from the left reservoir can jump into the double quantum dot system only when one electron has already left the system and was transferred to the right reservoir.

Finally, in order to show that pulse shaping can indeed lead to a remarkable enhancement of the photon assisted current through double
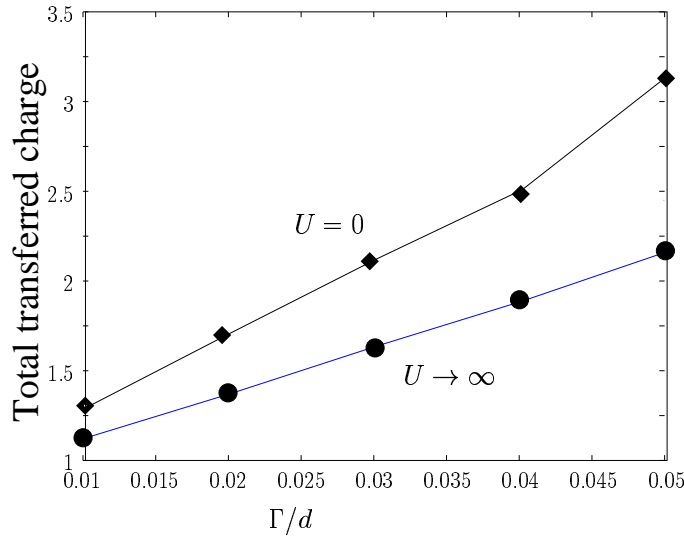
Figure 3.29: Dependence of the total transferred charge Q_T (diamonds) induced by the optimal pulse as a function of the coupling Γ to the reservoirs for $U = 0$. The circles represent the value of Q_T for $U \to \infty$.

Table 3.1: The total transferred charge $Q_T[V(t)]$ induced by different pulses of the same energy $E = 4.26E_0$. The coupling to the reservoirs is taken as $\Gamma = 0.01d$ and the interdot repulsion $U = 0$.

Pulse shape	Q_T
optimal pulse	1.29
rectangular pulse	0.85
Gaussian pulse	0.74
constant pulse	0.77

quantum dots, we indicate in Table [3.1] the values of the transferred charge Q_T for the coupling constant $\Gamma = 0.01d$ and pulses having different shapes $V(t)$ but carrying the same energy E. As expected, the optimal pulse found by the GA (already shown in Fig. [3.24]) induces clearly more transferred charge than pulses having other shapes. It is important to point out that the rectangular and Gaussian pulses mentioned in Table [3.1] are the fittest ones among rectangular and Gaussian pulses, respectively. Thus, the optimal pulse induces 1.74 times more transferred charge Q_T than the best Gaussian pulse, and 1.5 times than the best rectangular pulse.

This shows that the GA is a powerful method for a solution of the optimal control problem for the quantum systems during a finite time interval.

3.4 Explosion of Xe_N clusters

In this section we present results of our investigations of the Xe clusters explosion. Using a microscopic theoretical approach described in the Theory section [2.4] we perform quantum dynamical simulations of the ionization and explosion processes induced by intense femtosecond laser pulses. We show that the remarkable correlation between kinetic energy and charge of the produced ions observed in different experiments can be described as arising from the strongly inhomogeneous charge densities in the clusters, which are induced by the collective dynamics of the electrons after the laser excitation. With the help of the obtained results we suggest a simple classical model that explains known experimental data [17].

In the first subsection ionization and explosion dynamics were investigated. In the second subsection we study size and charge effects on the ejected ions kinetic energy distribution. In the third subsection we present a model of inhomogeneously charged cluster explosion in order to give a simple description of the experimental findings by Lezius et al. [17].

3.4.1 Ionization and explosion dynamics

Using the approach described in the section [2.4], we have performed calculations of the laser induced ionization and explosion dynamics of Xe_N clusters excited by intense femtosecond laser pulses.

First, we determine the ground state of the electronic and atomic structure. For this purpose we used a combined scheme of the Genetic algorithm [77] and simulated annealing [59] using as a fitness function the total energy of the system. Then Eqs. [2.53] and [2.54] have been numerically solved on a spatial grid. For the time propagation we use the split operator technique. For each cluster size we made at least ten runs to have a statistics related to fluctuations of intensity of the external laser field. In our simulations we use a square laser pulse with the intensity $I = 3.7 \times 10^{16} \text{W/cm}^2$ and the wavelength λ=800 nm, and having the pulse duration of 80 fs. In our simulations we obtain a strong ionization of the clusters and highly charged and energetic ions.

To illustrate the explosion dynamics we show in Fig. [3.30] the calculated electron charge density together with the positive nuclei potential (20 atoms in the cluster) after 20 fs laser excitation. The minima of the nuclei potential correspond to the positions of the individual nuclei. One can see that some fraction of the electron density moves outside the cluster. This is a clear manifestation that the cluster becomes charged. However, the nuclei position (except on the "surface" of the cluster, where the Coulomb repulsion is larger) remains unchanged. Fig. [3.31] displays a later stage of the cluster explosion when a significant fraction of electrons has left the cluster. The internuclear distance increases rapidly, indicating the
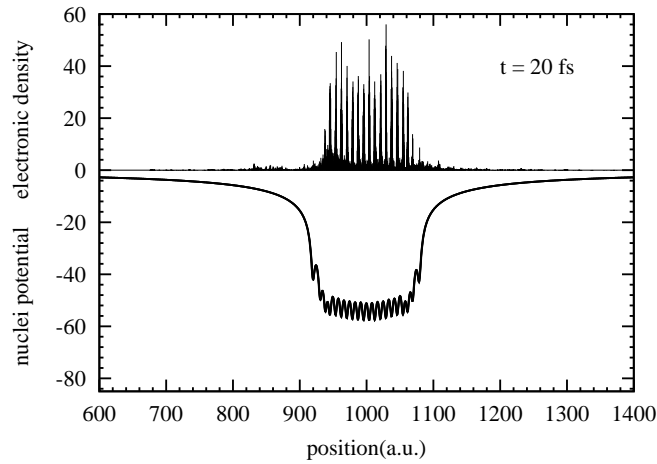
Figure 3.30: Snapshot of the electronic density (in arbitrary units) and nuclei potential (in arbitrary units) for the 20-atoms Xe cluster 20 fs after the pulse was applied. The spatial coordinate is given in Bohr radius a_0.

explosion of the cluster. One can estimate that the typical time scale for the cluster explosion is of the order of 100 fs. For our simulations we use the size of the box $L = 2000a_0$ ($a_0 = 1$ Bohr radius).

In order to characterize the collective motion of electrons we calculate the time-dependence of the dipole moment of the cluster during the action of the pulse. In our calculations we used the following definition of the
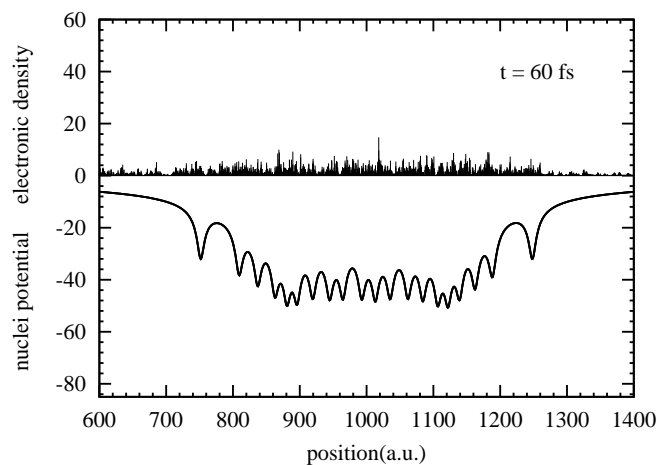

Figure 3.31: The same notation, as in Fig. [3.30], but 60 fs after the laser pulse was applied.

dipole moment:

$$d(t) = \int |\Psi(x,t)|^2 (x - x_0) dx, \qquad (3.13)$$

where x_0 is the coordinate of the cluster's center of mass. The integration is performed over the whole region of simulations. In Fig.[3.32] we show the result of calculations for the cluster size $N = 8$. Note the
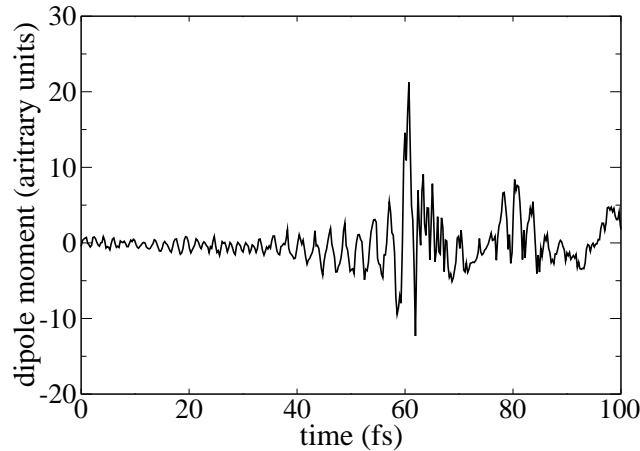

Figure 3.32: Oscillations of the dipole moment $d(t)$ of the cluster in time. The cluster size is $N = 8$. Note clear evidence of the resonance appears about 60 fs.

rapid increase of the amplitude of oscillations approximately at the moment corresponding to 60 fs after beginning of the excitation. Since the pulse amplitude is chosen to be a constant, one can assume that at 60 fs collective motion of electrons becomes resonant with oscillations of the external field.

3.4.2 Dependence of the kinetic energy distribution on the cluster size

In Fig. [3.33] we show the calculated mean and maximal kinetic energies of the ions after explosion as a function of cluster size.

Both energies exhibit a significant increase from few keV for relatively small clusters (with $N = 3 - 6$) up to few tens of keV for large clusters ($N = 25 - 30$). These results are a in qualitative agreement with the experimental findings [18]. Interestingly, the length of a Xe_{17} cluster is $\ell_{17} \approx 70\text{Å}$, which corresponds approximately to the diameter of the Xe_N clusters for which the experimental signal also start to exhibit high energetic ions [16]. Note, that there is a saturation of the maximal and mean

kinetic energies for cluster sizes $N \approx 20 - 25$ and then for larger clusters both energies start to decrease. The reason of the saturation effect is that larger clusters $N \geq 17$ explode more slowly and the resonance condition is satisfied after the pulse stops (after 80 fs). This effect was also observed experimentally [18].
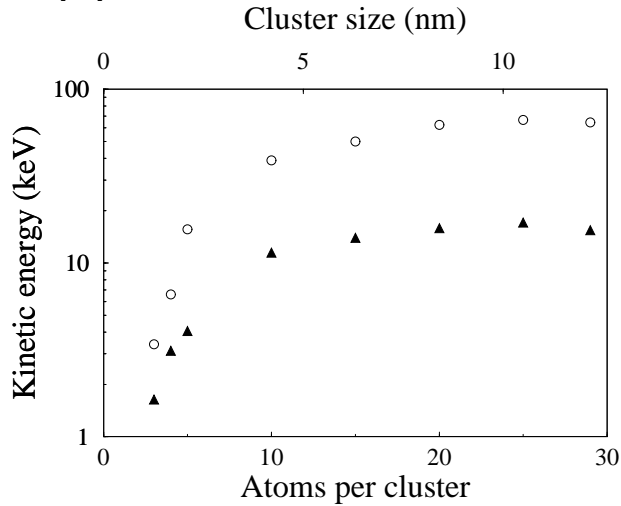

Figure 3.33: Calculated maximal (circles) and mean (triangles) kinetic energy of Xe^{q+} ions produced upon explosion of linear Xe_N clusters as a function of number of atoms N in the cluster. The size of the clusters is also indicated.

This is an indication that the 1D model yields a qualitatively correct description. However, the magnitude of our calculated energies is considerably smaller than were observed in experiments. This quantitative discrepancy is due to the 1D approximation, since a linear cluster of length ℓ contains much less atoms than the corresponding 3D cluster of diameter ℓ, which gives rise, when charged, to a much stronger repulsive potential.

Let us now study the correlation between the kinetic energy of the ejected ions and their charge state. We estimate charge of the ion using the following approximation. Shortly before the ion leaves the region of numerical simulations, we calculate the integral

$$Q = \int_{x_0 - \Delta R}^{x_0 + \Delta R} |\Psi(x, t_0)|^2 dx, \qquad (3.14)$$

where x_0 is a current position of the ion at the time moment t_0 and we choose $\Delta R = 4.2a_0$ that yields the value $Q = 54$ for each nucleus in the Xe_2 molecule at the equilibrium.

In Fig. [3.34(a)] we plot the kinetic energy E_{kin} of the produced ions as a function of their charge q for a cluster (chain) ensemble ranging in size from N = 3 to 26. In general, the most energetic ions are those coming from the surface of the cluster. Notice the remarkably strong correlation
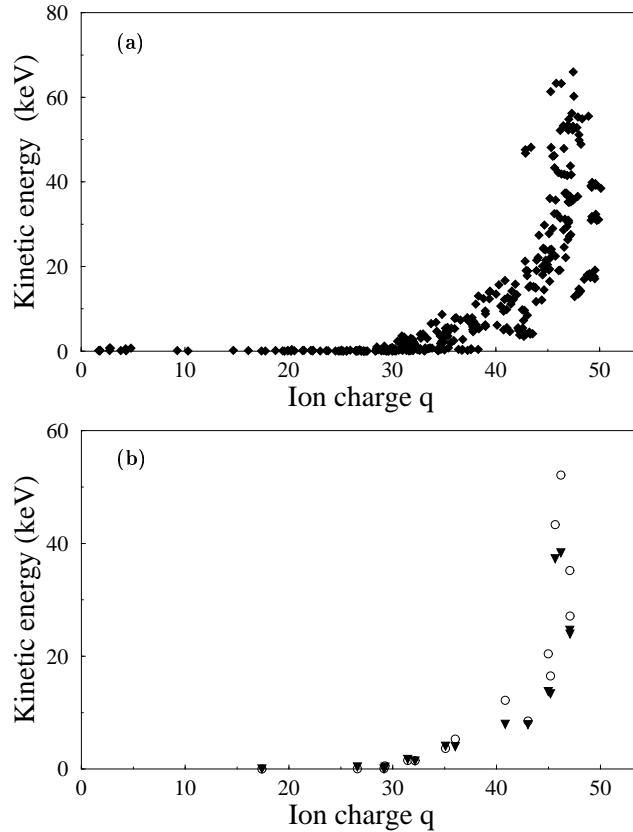
Figure 3.34: (a) Kinetic energy E_{kin} versus charge state q for Xe^{q+} ions emitted upon laser excitation of a distribution of Xe_N clusters. (b) E_{kin} versus q after explosion of a Xe_{16} cluster obtained from the full quantum mechanical simulation (circles) and from a classical pure Coulomb explosion model (triangles). Note the difference in the kinetic energy for large q referring to surface atoms originates from the electron pressure.

between the energies and charges of the produced ions for various cluster sizes as is found in experiment [17]. Note also, that the dependence of E_{kin} on q is neither linear as predicted by the pure "hydrodynamic" model nor quadratic as predicted by the pure Coulomb explosion approach. In fact Fig. [3.34(a)] shows much a more rapid nonlinear increase.

In order to quantify the contribution of the electron dynamics to the kinetic energy of the emitted ions (so called hydrodynamic mechanism) we performed test runs in which we analyzed the pure Coulomb explosion of the pre-charged cluster. As input for these simulations we used the charge distribution within the cluster obtained from the integration of equations of motion (see Eqs. [2.53] and [2.54]) until shortly before explosion, i.e. until stage (iii). In Fig. [3.34(b)] we show for Xe_{16} the resulting dependence of the kinetic energy E_{kin} vs the charge state q for pure Coulomb explosion calculations and for the case resulting from using Eqs. [2.53] and [2.54]

over the whole time-range.

From our simulations we found that the electron pressure does not accelerate ions which are close to the center of the cluster. In Fig. [3.34(b)] these ions have lower energy and charge state. A possible explanation of this result is that all forces which act on ions in the center of the cluster cancel each other. The pressure of hot electrons is much more efficient for the acceleration of highly charged ions at the surface. As seen in Fig. [3.34(b)] these ions have higher energy and charge state. The contribution of the electron pressure has clearly a nonlinear dependence on ion ion charge. The initial position of the ion in the cluster is significant.
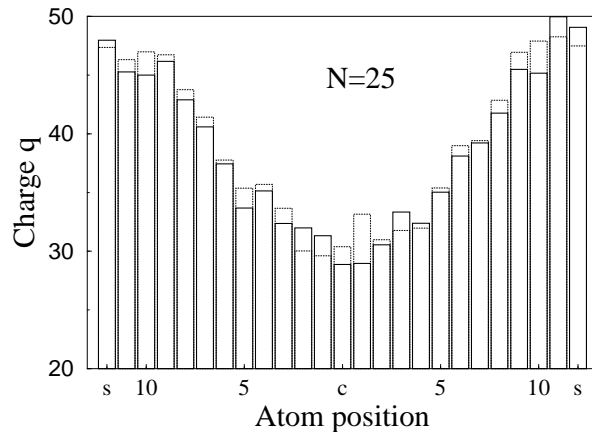

Figure 3.35: Charge q of the different ionized atoms in a Xe_{25} cluster immediately before the explosion. The solid and dotted lines refer to slightly different pulse intensities used in the simulations. Note the increase of the ionization from the center (c) to the surface (s).

From Fig. [3.34(b)] it becomes clear that in the last stage of the explosion process the quantum electron dynamics, which is absent in the pure Coulomb model, does only yield a contribution of about 20% to E_{kin} (see Fig. [3.34(b)]). This indicates that this dependence is completely determined during the stages (i) and (ii) (see Theory section [2.1]) and is a direct consequence of the charge distribution inside the cluster. Thus, our results for the 1D model show that the laser induced collective electron dynamics inside the cluster gives rise to a characteristic charge distribution in the cluster, which is responsible for the functional dependence of $E_{kin}(q)$.

In Fig. [3.35] we show a typical example of this characteristic charge distribution inside the cluster immediately before the explosion. The effect of the electron dynamics is to produce an inhomogeneous charge profile of the ionized atoms, which exhibits a minimum at the center and increases strongly for atoms close to the surface of the cluster. Such a charge distribution is an indication of strong nonlinear effects and might be produced

either by excitation of plasmons which decay via Landau damping at the surface, or by field induced electron tunneling, or by both mechanisms. For the case of 3D clusters we expect a similar effect of the electron dynamics on the charge distribution. It is important to point out, that although the electrons move mainly along the polarization-axis, there will be a strong coupling between the density oscillations along the different directions in this extremely nonlinear regime. As a consequence the charge distribution inside the cluster should become less anisotropic after stage (ii).

3.4.3 Isotropic inhomogeneous 3D Coulomb model

The previous discussion suggested that we can use the following simple 3D spherical model to describe the last explosion stage. We assume that a nonuniform, but isotropic charge distribution $\rho(r)$ has been created during the steps (i) and (ii) $\rho(r)$ gives rise to a Coulomb potential $U_{Coul}(r)$ at the distance r from the center of the cluster (see Fig. [3.36]):
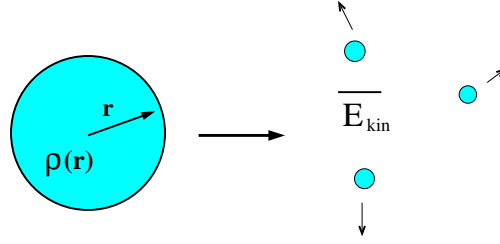

Figure 3.36: A simple model of the Coulomb explosion of the spherically symmetric charged cluster with the charge profile $\rho(r)$.

$$U_{Coul}(r) = 4\pi/r \int_0^r dr'\, r'^2 \rho(r'). \tag{3.15}$$

It must hold that

$$4\pi \int_0^R r'^2 dr'\, \rho(r') = \beta N_{at} Q, \tag{3.16}$$

where R is the cluster radius and $\beta \approx 0.4$ is the fraction of remaining electrons in the cluster, Q is the charge of the Xenon nucleus (Q=+54) and N_{at} the total number of atoms in the cluster. This will lead to a kinetic energy distribution of the form

$$E_{kin}(r) = U_{Coul}(r)\rho(r)V/N_{at}, \tag{3.17}$$

where $V = 4/3\pi R^3$ is the volume of the cluster shortly before explosion.

Using Eq. [3.17] we can now determine $\rho(r)$ from fitting the experimentally observed dependence $E_{kin}(q)$ for the highly energetic ions with
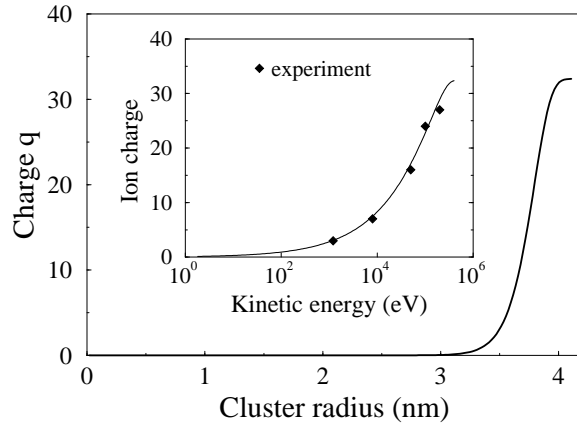
Figure 3.37: Charge profile inside a 3D spherical cluster derived from the experimental kinetic energy distribution of the highly energetic ions. Inset: fit of the experimental data measured in [17] assuming the inhomogeneous Coulomb explosion model.

$E_{kin} > 10^3$eV [17]. The result is shown in Fig. [3.37] . Note, that the ionic charge seems perfectly screened at the center of the cluster.

Interestingly the $\rho(r)$ derived from the experimental results shows the features predicted by the 1D model, namely strong inhomogeneous ionization and concentration of the ion charge near the surface.

The charge profile $\rho(r)$ in Fig. [3.37] exhibits also a surprising property. Since the positive charge is sufficiently large for $r > 3$ nm, this means that only clusters having initial diameter larger than 6 nm can contribute to the tail of the highly charged and energetic ions. This conclusion is in very good agreement with the observations of T. Ditmire and co-authors [16].